

---

# SUB-METRE LUNAR DEM GENERATION AND VALIDATION FROM CHANDRAYAAN-2 OHRC MULTI-VIEW IMAGERY USING OPEN-SOURCE PHOTOGRAMMETRY

---

A PREPRINT

 **Aaranay Aadi**

School of Computer Science and Engineering  
Manipal University Jaipur  
Jaipur, India  
aaranayaadi@gmail.com

 **Jai Singla**

Space Applications Centre (SAC)  
Indian Space Research Organisation (ISRO)  
Ahmedabad, India  
jaisingla@sac.isro.gov.in

 **Nitant Dube**

Space Applications Centre (SAC)  
Indian Space Research Organisation (ISRO)  
Ahmedabad, India  
nitant@sac.isro.gov.in

 **Oleg Alexandrov**

Intelligent Robotics Group  
NASA Ames Research Center  
Moffet Field, CA, USA  
oleg.alexandrov@nasa.gov

## ABSTRACT

High-resolution digital elevation models (DEMs) of the lunar surface are essential for surface mobility planning, landing site characterization, and planetary science. The Orbiter High Resolution Camera (OHRC) on board Chandrayaan-2 has the best ground sampling capabilities of any lunar orbital imaging currently in use by acquiring panchromatic imagery at a resolution of roughly 20–30 cm per pixel. This work presents, for the first time, the generation of sub-metre DEMs from OHRC multi-view imagery using an exclusively open-source pipeline. Candidate stereo pairs are identified from non-paired OHRC archives through geometric analysis of image metadata, employing baseline-to-height (B/H) ratio computation and convergence angle estimation. Dense stereo correspondence and ray triangulation are then applied to generate point clouds, which are gridded into DEMs at effective spatial resolutions between approximately 24 and 54 cm across five geographically distributed lunar sites. Absolute elevation consistency is established through Iterative Closest Point (ICP) alignment against Lunar Reconnaissance Orbiter Narrow Angle Camera (NAC) Digital Terrain Models, followed by constant-bias offset correction. Validation against NAC reference terrain yields a vertical RMSE of 5.85 m (at native OHRC resolution), and a horizontal accuracy of less than 30 cm assessed by planimetric feature matching.

**Keywords** Chandrayaan-2 · OHRC · digital elevation model · stereo reconstruction · photogrammetry · Community Sensor Model · Ames Stereo Pipeline · lunar terrain

## 1 Introduction

Digital Elevation Models (DEMs) of the lunar surface underpin a broad range of scientific investigations, including geomorphological mapping, impact crater morphometry, and slope hazard assessment for future robotic and human landing missions. The accuracy and resolution of a DEM fundamentally determines the scale of surface features that can be studied.

The primary source of high-resolution lunar topographic data has been the Lunar Reconnaissance Orbiter (LRO), in particular the Lunar Orbiter Laser Altimeter (LOLA) [Smith et al., 2010] and the Narrow Angle Camera (NAC) [Robinson et al., 2010]. NAC stereo-derived DEMs achieve resolutions of approximately 1–5 m per pixel depending on

imaging geometry and have proven highly valuable for detailed terrain studies. At the planetary scale, the SELENE Terrain Camera has also contributed global topographic models [Araki et al., 2009].

The Chandrayaan-2 Orbiter High Resolution Camera (OHRC) [Chowdhury et al., 2020] represents a qualitative advance in ground sampling capability, acquiring panchromatic imagery at approximately 25–30 cm per pixel from a 100 km orbit [Indian Space Research Organisation, 2019]. This resolution, roughly an order of magnitude finer than typical NAC DEMs, would allow DEM products capable of resolving boulder-scale topographic features and metre-scale slope variations. Such data are of direct relevance to landing site certification and rover traverse planning for future lunar surface missions. The geometric fidelity of OHRC imagery has previously been demonstrated for surface feature localisation, including reconstruction of the Chandrayaan-3 rover traverse path [Iyer et al., 2025].

Despite this potential, the use of OHRC imagery for DEM generation within open-source stereo pipelines remains limited. Two practical challenges have contributed to this. First, OHRC images are not acquired or distributed as explicit stereo pairs. As a result, suitable image combinations must be identified from orbital geometry and acquisition metadata, rather than being available a priori. Second, OHRC data formats and sensor models are not directly supported within commonly used tools such as the integrated software for imaging spectrometers (ISIS)[Gaddis et al., 1997] and Ames Stereo Pipeline (ASP)[Shean et al., 2016, Moratto et al., 2010, Beyer et al., 2018]. Recent open-source efforts have partially addressed this by enabling ingestion of OHRC data through PDS4-compatible workflows and corresponding CSM-based camera models, allowing stereo reconstruction to be carried out within a standard framework.

In this work, we build on these developments to generate and analyse DEMs from OHRC stereo imagery across multiple lunar regions. The emphasis is on evaluating how reliably sub-metre terrain structure can be recovered in practice, and on assessing the geometric and elevation consistency of the resulting products with respect to reference datasets. The reconstructed DEMs are produced at resolutions between 24 and 54 cm and show clear preservation of fine-scale surface morphology.

The contributions of this work are as follows:

- Reconstruction of lunar DEMs from Chandrayaan-2 OHRC imagery at sub-metre spatial resolution (24–54 cm).
- Demonstration of an end-to-end open-source workflow for OHRC stereo processing.
- Quantitative and qualitative evaluation of the reconstructed DEMs against reference NAC-derived terrain for geometric consistency and elevation accuracy.
- Post-processing of DEM products, including hole-filling and mosaicing, to improve completeness of the reconstructed regions.

## 2 Related Work

### From Laser Altimetry to High-Resolution Stereo Photogrammetry

The history of lunar topographic mapping reflects a progressive shift from global laser altimetry to dense regional photogrammetry, driven by the increasing demand for terrain products at the scale of landing hazards. Early global coverage was established by the SELENE Laser Altimeter (LALT) and consolidated by LOLA, which provided a globally consistent vertical datum at 30 m horizontal resolution [Smith et al., 2010]. While both instruments offer centimetre-level ranging precision, their across-track shot spacing, that is on the order of 1–4 km at the equator for LOLA, fundamentally limits their utility for dense topographic mapping [Barker et al., 2016]. The SLDEM2015 product, which fuses LOLA altimetry with SELENE Terrain Camera (TC) imagery, achieves approximately 60 m horizontal resolution [Barker et al., 2016], which remains insufficient for decimeter-scale hazard identification.

Stereo photogrammetry fills this gap by exploiting image pairs acquired from different viewing directions to reconstruct surface geometry at the spatial resolution of the imaging sensor. The geometric principles underlying stereo reconstruction, such as image matching, epipolar rectification, disparity estimation, and ray triangulation, are well established [Hartley and Zisserman, 2003], and their application to planetary remote sensing has been demonstrated across a wide range of missions and sensors. For Mars, the combination of HiRISE (0.25 m/pixel) and the Context Camera (CTX, 6 m/pixel) on the Mars Reconnaissance Orbiter has established a precedent for nested-resolution mapping, in which CTX DEMs provide regional context for HiRISE samples at the scale of boulders and slopes [Hepburn et al., 2019]. A similar multi-resolution approach is now achievable on the Moon using LRO NAC stereo at 1–2 m and OHRC at 25–30 cm, though the latter has not previously been demonstrated.

## Open-Source Photogrammetry Pipelines

The Ames Stereo Pipeline (ASP) [Moratto et al., 2010, Shean et al., 2016, Beyer et al., 2018] has been the community standard for planetary stereo DEM production for over a decade, providing an integrated suite of tools for radiometric normalisation, feature matching, bundle adjustment, dense disparity estimation, ray triangulation, and DEM gridding. ASP is built on the Vision Workbench library and relies on ISIS [Gaddis et al., 1997] for planetary-specific data ingestion and SPICE-based ephemeris and orientation (spiceinit) processing [Stathopoulou et al., 2019]. Successful applications of this pipeline include HiRISE stereo on Mars [Kirk et al., 2008], LRO NAC stereo on the Moon [Beyer et al., 2018], and imagery from a growing range of international missions.

A significant recent development in the ASP ecosystem is the adoption of the Community Sensor Model (CSM) [Community Sensor Model Working Group, 2015] and the Abstraction Layer for Ephemerides (ALE) [Laura et al., 2020] as a more general mechanism for sensor description. CSM-based camera models decouple the stereo pipeline from the legacy ISIS internal camera models, enabling ASP to handle pushbroom sensors from international missions — including those not originally designed with ASP compatibility in mind — without requiring instrument-specific code within the core pipeline [Liu et al., 2024]. This architectural shift is directly relevant to the present work: the OHRC sensor model is implemented as a CSM plugin, allowing standard ASP processing once the ISD file is generated via ALE.

## Lunar DEM Products and the Sub-Metre Gap

The highest-resolution publicly available lunar DEMs are derived from LRO NAC stereo pairs, typically at 1–2 m post spacing [Beyer et al., 2018]. These products have proven highly valuable for detailed crater morphometry and slope mapping, but their resolution remains insufficient for identifying decimeter-scale surface hazards such as rocks, hollows, and regolith texture variations that are operationally relevant for landing site safety [Barker et al., 2016]. Coverage at the Lunar South Pole (LSP) is further constrained by the extreme illumination geometry: near-polar imagery frequently contains large shadow regions that frustrate stereo matching, and the near-nadir viewing geometry of LRO NAC at high latitudes weakens the stereo convergence angle, reducing height sensitivity [Liu et al., 2024].

The OHRC instrument, with a GSD of 25–30 cm, occupies the sub-metre niche left unfilled by existing products. While LRO NAC offers broad coverage, its resolution ceiling of approximately 0.5 m per pixel (in the highest-resolution mode) remains coarser than OHRC by a factor of roughly two, and the strip-wise geometry of NAC acquisition makes it less well-suited to targeted high-fidelity site surveys [Liu et al., 2024]. A preliminary report by Gupta et al. [2021] suggested the feasibility of DEM generation from OHRC imagery but did not provide a verifiable methodology or sub-metre results. No peer-reviewed, openly reproducible sub-metre DEM products derived from Chandrayaan-2 OHRC data have been published.

## Stereo Pair Identification from Non-Paired Archives

Unlike dedicated stereo missions such as HRSC on Mars Express, which acquire simultaneous multi-angle imagery in a single pass, OHRC operates in a single-strip nadir-imaging mode. Viable stereo combinations must therefore be identified retrospectively from the image archive using geometric metadata. This “opportunistic stereo” approach has precedent in the context of historical satellite imagery and for Mars HiRISE [Kirk et al., 2008], where overlapping strips acquired on different orbital passes are evaluated for stereo suitability.

The primary geometric quality indicators for a candidate stereo pair are the overlap fraction, the illumination similarity between acquisitions (quantified by differences in solar incidence angle and azimuth), and the stereo strength as expressed by the baseline-to-height (B/H) ratio [Becker et al., 2015]. For automated dense matching, a B/H ratio between 0.5 and 1.0 is generally considered optimal: ratios below approximately 0.2 result in poor vertical precision because the height error scales as  $\Delta h \approx \text{GSD}/(B/H)$ , while ratios above approximately 1.2 introduce excessive perspective distortion and parallax that causes systematic failure in dense matching algorithms [Hasegawa et al., 2000, Toutin, 2002]. Illumination consistency is a further constraint specific to lunar stereo: because the Moon lacks an atmosphere, surface brightness is dominated by solar incidence angle, and pairs with large differences in solar geometry will exhibit photometric disparities that degrade correspondence quality. Studies on PlanetScope multi-view imagery have shown that even pairs with weak B/H ratios can yield sub-metre vertical accuracy when image texture is high [Ghuffar, 2018], but on the largely textureless highland regolith this condition does not generally hold, making shadow-tip extent a practical additional selection criterion [Becker et al., 2015].

Table 1: OHRC image dataset: acquisition locations and native image ground sampling distances. All Product IDs share the common prefix `ch2_ohr_nrp_`.

Region	Approx. Location	Product ID (Image 1) <code>ch2_ohr_nrp_...</code>	Product ID (Image 2) <code>ch2_ohr_nrp_...</code>	GSD <sub>1</sub> (cm/px)	GSD <sub>2</sub> (cm/px)
1	~69°S, 32°E	20240425T1209509264	20240425T1406019344	0.26	0.26
2	~5°N, 234°E	20220914T1033119094	20220914T0835371412	0.32	0.32
3	~69°S, 342°E	20230303T0350447888	20230303T0152168201	0.25	0.25
4	~13°S, 25°E	20210402T0155096873	20210401T2200364910	0.26	0.26
5	~4°N, 230°E	20220321T0525226030	20220321T0326369085	0.19	0.19

### 3 Dataset

OHRC images used in this study were obtained from the Chandrayaan-2 Map Browse facility of the Indian Space Research Organisation (ISRO). Each image is distributed in PDS4 format, consisting of a binary image file accompanied by an XML label containing instrument metadata, spacecraft state vectors, and imaging geometry parameters.

OHRC raw (uncalibrated) data products were used throughout this study in preference to the calibrated data products also distributed by ISRO. This choice was made for two reasons. First, ASP performs its own intensity normalisation prior to stereo matching. Specifically, a per-image normalisation to a mean  $\pm 2\sigma$  range, rather than a full photometric calibration; since radiometric calibration typically applies a scaling and a mildly non-linear response correction, the pipeline is expected to perform comparably on either calibrated or uncalibrated input. Second, the accuracy of the stereo-derived elevation model depends on the geometric fidelity of the camera model, which is encoded in the SPICE kernels and CSM sensor description, rather than on radiometric correction; using raw data therefore incurs no penalty in terms of the geometric quality of the final DEM.

Spacecraft orientation and position data required to reconstruct the camera geometry are provided through SPICE kernels [Acton, 1996] distributed via the ISRO Space Science Data Centre (ISSDC) PRADAN archive. These kernels encode spacecraft ephemeris (SPK), spacecraft orientation (CK), instrument parameters (IK), and planetary reference frames (PCK/FK) as a function of time.

Reference terrain data used for absolute alignment and hole-filling are NAC-derived Digital Terrain Models from the LRO archive, available at 1–2 m resolution.

Table 1 summarises the five stereo pairs used in this study, including the product identifiers of each constituent image and their native ground sampling distances as reported in the PDS4 XML metadata. Region 5, which exhibits the highest B/H ratio and the most extreme convergence geometry of the dataset, is discussed separately in Section 6.

## 4 Methodology

The processing chain comprises six main stages: (1) camera geometry initialisation, (2) stereo pair identification, (3) bundle adjustment, (4) dense stereo reconstruction and point cloud generation, (5) DEM gridding, and (6) post-processing including absolute alignment, offset correction, hole-filling, and mosaicing. Each stage is described below. The complete workflow is illustrated in Fig. 1.

### 4.1 OHRC Data Ingestion and SPICE Kernel Preparation

Ingestion of OHRC data into ASP begins with the acquisition and preparation of all relevant SPICE kernels from the ISSDC PRADAN archive. The kernel set required for OHRC comprises the spacecraft trajectory kernel (SPK), the attitude and pointing kernel (CK), the instrument kernel (IK) encoding the OHRC focal geometry, and the planetary constants and frame kernels (PCK and FK). Once downloaded, the kernels must be catalogued into an ISIS-format database before they can be used for camera initialisation. This is accomplished using `kerneldbgen`, an ISIS utility that parses each kernel file and writes an indexed `.db` file recording the kernel type, coverage interval, and file path. ISIS subsequently queries these database files by image acquisition time to select the correct kernels during `spiceinit`.

Native support for the Chandrayaan-2 OHRC instrument was not available in any stable release of ISIS at the time this work began. Sensor model support for OHRC was developed through active engagement with the open-source ISIS and ALE communities, resulting in contributions to the ISIS development branch that enabled correct ingestion and camera geometry initialisation for OHRC data products. Initial DEM results were produced in November 2025 using

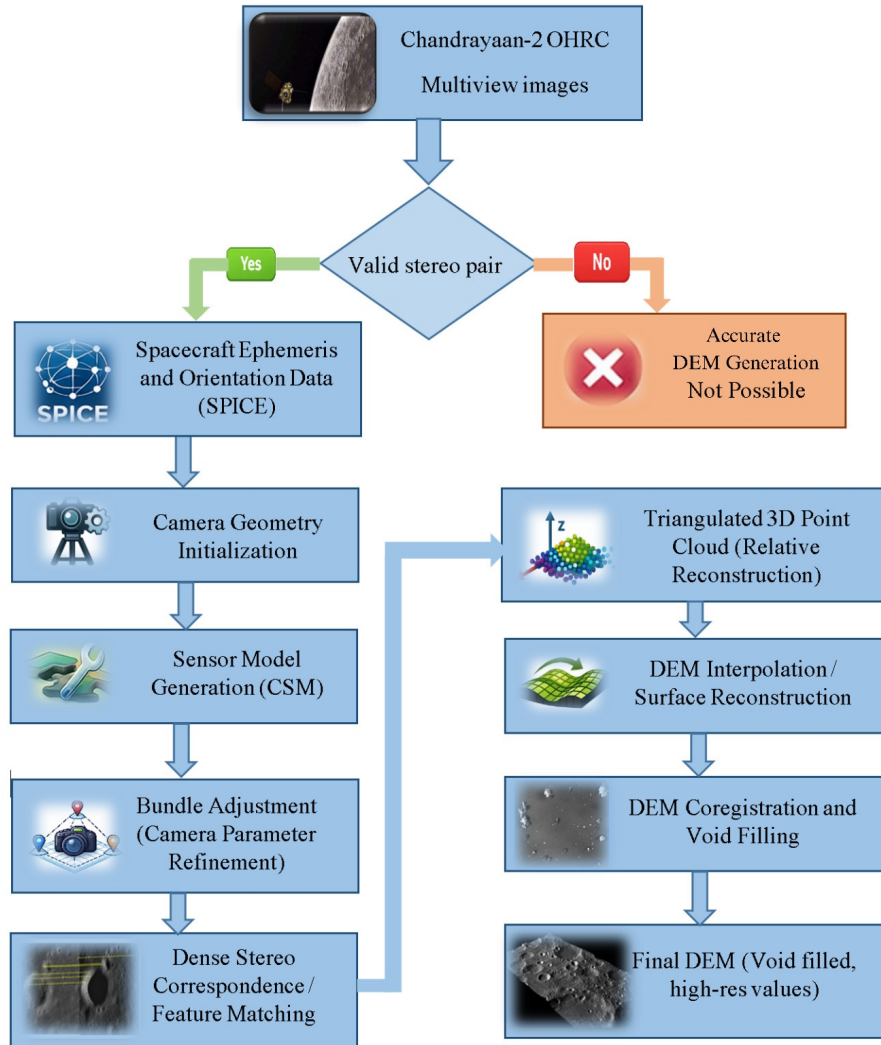


Figure 1: Overview of the OHRC DEM generation pipeline. Stages proceed from multi-view OHRC imagery and stereo pair selection through camera geometry initialisation, sensor model generation (CSM), bundle adjustment (camera parameter refinement), dense stereo correspondence and feature matching, triangulated 3D point cloud reconstruction, DEM interpolation and surface reconstruction, and finally DEM co-registration and void filling to yield the final terrain product.

ISIS compiled from source against this development branch using CMake. As of January 2026, the OHRC-capable ISIS build has been made publicly available through the official ISIS distribution, meaning the compilation-from-source step described here is no longer required for future users. This community-driven development pathway represents a direct and lasting expansion of the open-source planetary photogrammetry toolchain.

## 4.2 Camera Geometry Initialisation and ASP Compatibility

OHRC imagery is distributed in PDS4 format, which is not natively supported by ASP’s standard import routines. A dedicated PDS4 import template was developed to map OHRC-specific metadata fields to ASP’s internal ISIS cube format. This template defines the instrument line and sample dimensions, exposure parameters, and the mapping between XML label fields and ISIS keyword groups, enabling ISIS to correctly ingest OHRC image products.

Following import, SPICE kernels are called on each ISIS cube to attach spacecraft position and pointing information from the prepared SPICE database to the image label. The camera projection for a surface point  $P$  in the lunar

body-fixed frame is then modelled as [Hartley and Zisserman, 2003]:

$$\mathbf{p} = K [R \ \mathbf{t}] \mathbf{P} \quad (1)$$

where  $K$  is the intrinsic calibration matrix encoding focal length and principal point,  $R$  is the rotation matrix derived from CK kernel data, and  $\mathbf{t}$  is the translation vector from SPK ephemeris data.

To enable open-source photogrammetric processing, camera models are generated in the Community Sensor Model (CSM) format [Community Sensor Model Working Group, 2015] using the ALE (Abstraction Layer for Ephemerides) library [Laura et al., 2020]. This utility reads the SPICE-initialised ISIS cube and produces a JSON-format Instrument Support Data (ISD) file describing the complete sensor geometry required by ASP. Enabling this pipeline for OHRC required the development of a CSM sensor model configuration not previously available for this instrument.

### 4.3 Stereo Pair Identification

Because OHRC images are not acquired or catalogued as stereo pairs, viable stereo combinations must be identified from scratch using geometric parameters extracted from image XML metadata. Two images of the same surface are considered a candidate stereo pair if their relative viewing geometry satisfies constraints on the baseline-to-height ratio and the convergence angle.

The baseline  $B$  between two acquisitions is the distance between the spacecraft positions  $\mathbf{S}_1$  and  $\mathbf{S}_2$  at the time of each image:

$$B = \|\mathbf{S}_1 - \mathbf{S}_2\| \quad (2)$$

The baseline-to-height ratio is then

$$\frac{B}{H} = \frac{\|\mathbf{S}_1 - \mathbf{S}_2\|}{H} \quad (3)$$

where  $H$  is the spacecraft altitude above the surface. This ratio is a standard metric for stereo quality: values that are too low yield poor height sensitivity, while values that are too high cause large radiometric disparities that degrade matching [Toutin, 2002]. For spaceborne stereo, a B/H between 0.3 and 1.0 is generally considered optimal, though values up to approximately 1.2 have been reported as usable [Kirk et al., 2008].

The convergence angle  $\theta$  between the two viewing directions  $\hat{\mathbf{v}}_1$  and  $\hat{\mathbf{v}}_2$  is

$$\theta = \cos^{-1}(\hat{\mathbf{v}}_1 \cdot \hat{\mathbf{v}}_2) \quad (4)$$

For a pushbroom sensor observed from altitude  $H$  with baseline  $B$ , the convergence angle is related to the B/H ratio approximately as

$$\theta \approx 2 \arctan\left(\frac{B/H}{2}\right) \quad (5)$$

This approximation [Kirk et al., 2008] was used to estimate convergence angles for all candidate pairs in this study. The expected height precision (EP) of the resulting DEM scales inversely with the convergence angle as

$$\text{EP} \approx \frac{\rho}{\tan \theta} \quad (6)$$

where  $\rho$  is the image matching precision in pixels [Toutin, 2002].

Candidate pairs were identified by searching for OHRC images with overlapping ground footprints acquired within temporal windows short enough to ensure consistent surface illumination. B/H ratios and convergence angles were computed for all footprint-overlapping pairs and filtered against the geometric thresholds described above. The five stereo pairs selected for this study and their stereo geometry parameters are listed in Table 2.

### 4.4 Bundle Adjustment

Even with accurately initialised SPICE-based camera models, residual pointing errors between stereo images introduce systematic offsets that degrade reconstruction accuracy. Bundle adjustment jointly refines the camera parameters and the positions of matched feature points to minimise overall geometric inconsistency.

The objective minimised during bundle adjustment is the reprojection error summed over all matched tie points, wrapped in a robust cost function to attenuate the influence of outliers:

$$E = \sum_{i=1}^N \rho\left(\|\mathbf{p}_i - \hat{\mathbf{p}}_i(\mathbf{C}, \mathbf{X}_i)\|^2\right) \quad (7)$$

where  $\mathbf{p}_i \in \mathbb{R}^2$  is the observed image coordinate of tie point  $i$ , and  $\hat{\mathbf{p}}_i$  is its reprojection given the current camera parameters  $\mathbf{C}$  and 3D point position  $\mathbf{X}_i$ . The function  $\rho(\cdot)$  is a robust Cauchy loss,

$$\rho(s) = c^2 \log \left( 1 + \frac{s}{c} \right), \quad (8)$$

where  $c$  is a scale parameter controlling the influence of large residuals. This formulation down-weights outliers arising from mismatched tie points and improves the stability of the bundle adjustment solution. Optimisation was carried out using the Levenberg–Marquardt solver (implemented in the Google Ceres library [Agarwal et al., 2022]) over up to 100 iterations. In addition to the reprojection term, ASP’s bundle adjustment incorporates a ground constraint based on triangulated point positions to prevent the camera solution from drifting away from the initial SPICE geometry, and optionally allows the user to specify a camera position uncertainty constraint. The refined camera states are saved and used as the adjusted pointing model for all subsequent stereo processing.

#### 4.5 Dense Stereo Reconstruction

Following bundle adjustment, dense stereo matching is performed to compute per-pixel disparities between the rectified image pair. The disparity field  $\mathbf{d}(u, v)$  encodes the horizontal displacement between corresponding pixels in the two images. The default stereo algorithm in ASP is a block-matching approach based on normalised cross-correlation, which was used in this study.

While ASP provides the More Global Matching (MGM) method of Facciolo et al. [2015] as a more advanced alternative, block matching was found to be sufficient for OHRC imagery due to its high spatial resolution and strong local contrast, which provide reliable matching cues at the native scale. Additionally, the lower computational and memory overhead of block matching makes it well-suited for processing large OHRC scenes without compromising reconstruction quality in well-textured regions.

Each matched pixel pair  $(\mathbf{p}_1, \mathbf{p}_2)$  defines a pair of viewing rays from cameras  $C_1$  and  $C_2$ . The 3D position of the corresponding surface point is determined by ray triangulation:

$$\mathbf{X} = \text{Triangulate}(C_1, C_2, \mathbf{p}_1, \mathbf{p}_2) \quad (9)$$

where  $C_1$  and  $C_2$  are the refined camera projection matrices from bundle adjustment and  $\mathbf{p}_1, \mathbf{p}_2$  are the matched image coordinates. In practice the two rays are not exactly coplanar, so  $\mathbf{X}$  is computed as the midpoint of the shortest segment connecting the two rays. Applying this over all matched pixels produces a dense 3D point cloud representing the lunar surface.

#### 4.6 DEM Gridding

The irregular 3D point cloud is rasterised onto a regular geographic grid to produce the DEM. For each grid cell at  $(x, y)$ , the elevation is estimated by interpolating over neighbouring point cloud samples:

$$z(x, y) = \frac{\sum_i w_i z_i}{\sum_i w_i} \quad (10)$$

where  $z_i$  are the elevations of points within the interpolation kernel and  $w_i$  are distance-based weights. Grid cells for which no point cloud samples fall within the search radius are marked as no-data and subsequently addressed in the hole-filling stage. DEM gridding was performed using `point2dem` within ASP, with the output projected in a stereographic projection appropriate to the region of interest.

#### 4.7 Absolute Elevation Alignment with NAC Reference

The DEM produced directly from stereo reconstruction represents elevations in a local reference frame and may carry a global offset relative to the lunar body-fixed coordinate system due to residual camera geometry errors. To establish absolute elevation consistency, the reconstructed OHRC DEM is aligned with a co-located NAC DTM using an Iterative Closest Point (ICP) approach [Besl and McKay, 1992].

ICP iteratively estimates the rigid transformation

$$\mathbf{P}' = \mathbf{R}\mathbf{P} + \mathbf{T} \quad (11)$$

that minimises the mean squared distance between the OHRC point cloud and the NAC reference surface:

$$\arg \min_{R, \mathbf{T}} \frac{1}{N} \sum_{i=1}^N \|\mathbf{P}'_i - \mathbf{Q}_i\|^2 \quad (12)$$

where  $\mathbf{Q}_i$  are the nearest-neighbour correspondences on the NAC surface and  $R \in SO(3)$ ,  $\mathbf{T} \in \mathbb{R}^3$ . The estimated transform was applied to re-project the OHRC point cloud before final DEM gridding.

#### 4.8 DEM Offset Correction

Following ICP alignment, terrain profile comparison between the OHRC DEM and the NAC DTM may reveal a residual constant vertical bias arising from systematic errors in the spacecraft altitude solution not fully captured by ICP. The corrected elevation is

$$z_{\text{corrected}}(x, y) = z_{\text{DEM}}(x, y) - \Delta z \quad (13)$$

where  $\Delta z$  is the mean vertical offset estimated from profile analysis along representative terrain transects (using QGIS). Only constant-offset corrections (i.e., uniform vertical shifts with no tilt component) are applied; tilt residuals, if present, are addressed by the ICP step.

#### 4.9 Hole Filling Using NAC Terrain Data

Stereo reconstruction at sub-metre resolution produces no-data regions wherever image matching fails, typically in shadow-affected areas or surfaces with insufficient photometric texture. To produce a continuous terrain model, missing elevations are filled using the aligned NAC DTM. Let  $D_{\text{OHRC}}(x, y)$  denote the OHRC-derived elevation and  $D_{\text{NAC}}(x, y)$  denote the reference elevation. The merged elevation is defined as

$$D(x, y) = \begin{cases} D_{\text{OHRC}}(x, y), & \text{if } D_{\text{OHRC}}(x, y) \text{ is valid} \\ D_{\text{NAC}}(x, y), & \text{otherwise} \end{cases} \quad (14)$$

This substitution preserves OHRC-derived elevations wherever available, falling back to NAC data only in regions where stereo reconstruction failed.

#### 4.10 Priority-Based DEM Mosaicing

Where multiple DEM tiles from adjacent or overlapping stereo pairs cover a common region, the tiles are combined into a single continuous product. A priority-based blending strategy is applied using `dem_mosaic`, which assigns higher priority to OHRC-derived elevations over NAC terrain within a configurable blending-length transition zone. The final merged elevation at  $(x, y)$  is given by

$$D_{\text{final}}(x, y) = \alpha(x, y) D_{\text{OHRC}}(x, y) + (1 - \alpha(x, y)) D_{\text{NAC}}(x, y) \quad (15)$$

where  $\alpha(x, y) \in [0, 1]$  is a spatially varying weight that equals 1 in regions with full OHRC coverage and transitions smoothly to 0 at the boundaries of the OHRC footprint, ensuring artefact-free blending. Within OHRC-covered regions  $\alpha = 1$  and the equation reduces to the hole-filling formulation above. The blending transition length was set to 14 pixels.

## 5 Results

The proposed workflow was applied to five lunar regions spanning a range of latitudes and terrain types. Table 2 summarises the computed B/H ratios, convergence angles, and the spatial resolutions of the generated DEMs. Convergence angles were computed from B/H ratios using Eq. (5); for Region 5 the directly measured angle of  $\sim 61^\circ$  is reported, as the approximation underestimates the true angle at high B/H values.

B/H ratios across the five pairs range from 0.396 (Region 1) to 1.161 (Region 5), corresponding to convergence angles of approximately  $22^\circ$  to  $61^\circ$ . Regions 1–4 all fall within the commonly recommended B/H range of 0.3–1.0 [Toutin, 2002] and produced DEMs with satisfactory spatial completeness.

Completed DEMs for Regions 1–4 achieve effective spatial resolutions between 31 cm and 54 cm, representing the highest-resolution DEM products reported from Chandrayaan-2 OHRC data to date and covering four geographically distributed sites. Region 5, while yielding the finest nominal grid spacing (24 cm), exhibits a substantially elevated void fraction and is discussed as a limiting case in Section 6. The variation in resolution across regions reflects differences in

Table 2: Stereo geometry and generated DEM characteristics for each region, ordered by increasing B/H ratio.

Region	Approx. Location	B/H Ratio	Conv. Angle ( $^{\circ}$ )	DEM Resolution
1	$\sim 69^{\circ}\text{S}, 32^{\circ}\text{E}$	0.396	$\sim 22^{\circ}$	31 cm
2	$\sim 5^{\circ}\text{N}, 234^{\circ}\text{E}$	0.414	$\sim 23^{\circ}$	54 cm
3	$\sim 69^{\circ}\text{S}, 342^{\circ}\text{E}$	0.559	$\sim 31^{\circ}$	30 cm
4	$\sim 13^{\circ}\text{S}, 25^{\circ}\text{E}$	0.877	$\sim 47^{\circ}$	48 cm
5	$\sim 4^{\circ}\text{N}, 230^{\circ}\text{E}$	1.161 <sup>‡</sup>	$\sim 61^{\circ}$ <sup>†</sup>	24 cm

<sup>†</sup> Directly measured; the approximation of Eq. (5) underestimates  $\theta$  at high B/H.

<sup>‡</sup> High void fraction; see Section 6 for details regarding performance at high B/H.

OHRC image sampling at acquisition time. Alignment with NAC DTMs established absolute elevation consistency, and priority-based mosaicing produced continuous terrain products.

The five DEMs are shown together in Fig. 2. Regions 2 and 4 exhibit well-filled terrain models with minimal void fraction. Region 1 retains some unfilled areas owing to gaps in the corresponding NAC DTM used for infill. Region 3 had no NAC reference available and is therefore presented without void filling.

Figs. 3 and 4 present side-by-side hillshade comparisons of the OHRC-derived DEM and the NAC DTM at four randomly selected sites drawn from Regions 1 and 4 respectively, illustrating the close visual agreement in terrain morphology between the two products at sub-metre scales.

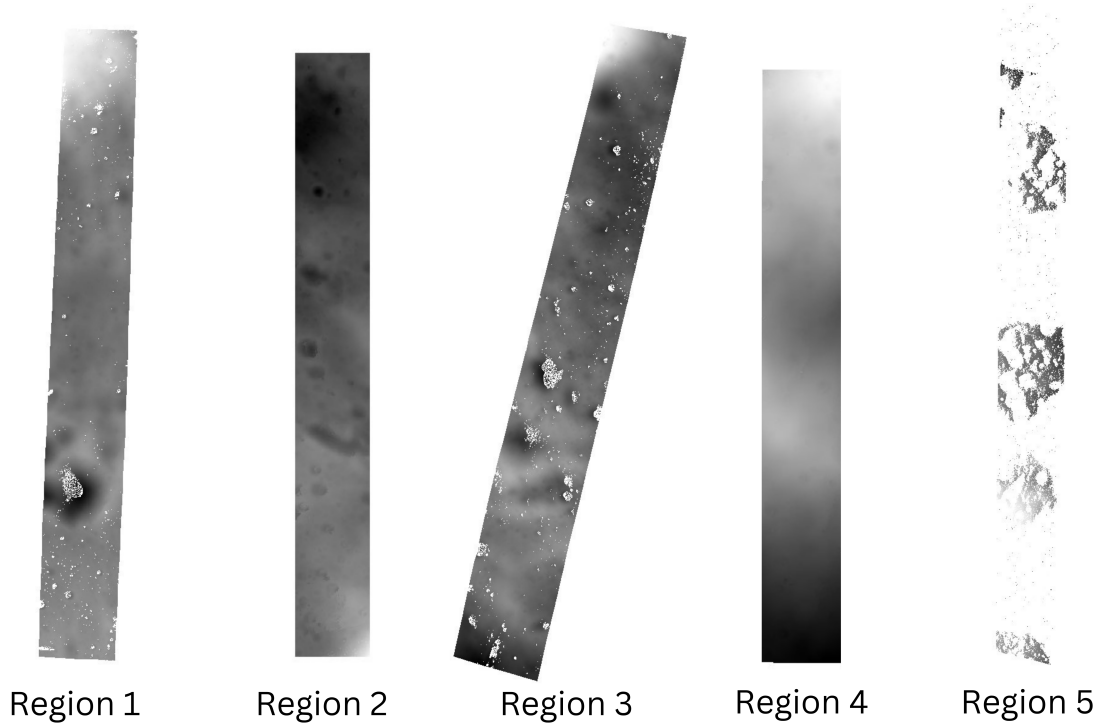


Figure 2: DEMs for all five reconstructed regions. Region 5 is included for completeness; its high void fraction reflects the limiting effect of an extreme convergence angle ( $\theta \approx 61^{\circ}$ ) on semi-global matching performance, as discussed in Section 6. Regions 2 and 4 have well-filled DEMs with minimal voids. Region 1 was not fully filled using NAC due to the presence of holes in the corresponding NAC DTM. Region 3 has no corresponding NAC reference available.

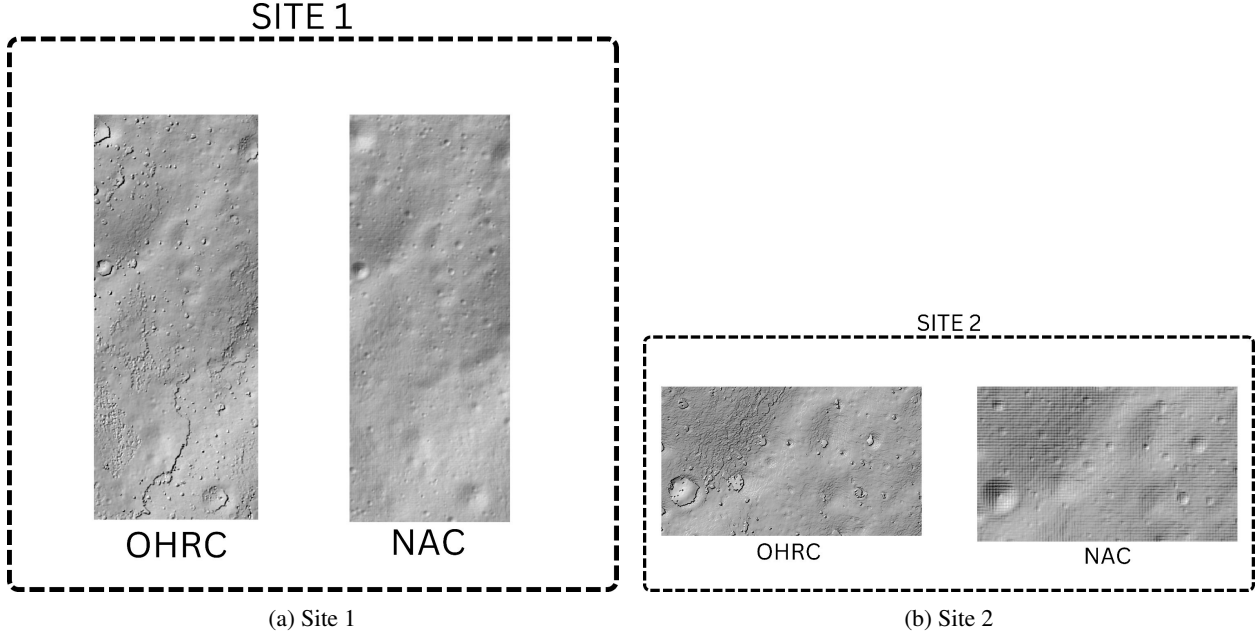


Figure 3: Visual feature comparison of OHRC generated DEM vs NAC DTM (both hillshaded) for Sites 1 and 2, randomly selected from Region 4.

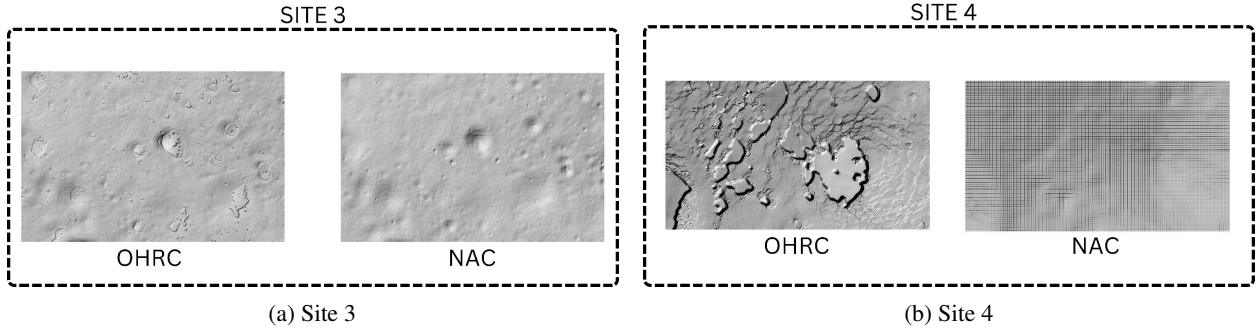


Figure 4: Visual feature comparison of OHRC generated DEM vs NAC DTM (both hillshaded) for Sites 3 and 4, randomly selected from Region 2.

### 5.1 Validation Against NAC Reference Terrain

Metrological validation of the generated DEMs was carried out by comparing elevation profiles extracted from the OHRC DEM against co-located profiles from the NAC DTM reference. Profile transects were drawn across representative terrain features using QGIS, including crater rims and flat mare surfaces, ensuring that the comparison spans both high-relief and low-relief terrain.

Let  $z_{\text{OHRC}}(s)$  and  $z_{\text{NAC}}(s)$  denote the elevation values along a profile parameterised by arc length  $s$ . The vertical discrepancy at each sample is

$$\delta(s) = z_{\text{OHRC}}(s) - z_{\text{NAC}}(s) \quad (16)$$

The root-mean-square error (RMSE) of the vertical difference over the profile is

$$\text{RMSE}_v = \sqrt{\frac{1}{N} \sum_{i=1}^N \delta(s_i)^2} \quad (17)$$

Across the validated regions (Regions 1, 2, and 4), the vertical RMSE values are reported in Table 3. It should be noted that these figures reflect a comparison between the OHRC DEM at its native sub-30 cm resolution and the NAC DTM at approximately 3 m posting. A like-for-like vertical accuracy assessment, in which the OHRC DEM was downsampled to NAC resolution prior to differencing, was also conducted, yielding roughly the same values. Region 3 does not have a corresponding NAC reference and could not be evaluated. Region 5 was excluded from the primary validation owing to its elevated void fraction.

Table 3: Vertical RMSE by region (computed from the standard deviation of elevation residuals after bias correction, compared against the NAC DTM).

Region	RMSE (cm)
1	298.96
2	850.42
3	— (no NAC DTM available)
4	606.66
5	— (excluded; high void fraction)
<b>Mean (Regions 1, 2, 4)</b>	<b>585.35 <math>\approx</math> 5.85 m</b>

Horizontal accuracy was assessed independently of the vertical comparison by identifying morphologically distinct surface features, including small crater rims and sharp ridge crests, that are unambiguously localised in both the OHRC DEM hillshade and the NAC DTM hillshade. Between 5 and 10 such features were identified per validated region, and their planimetric centroids were measured in QGIS. The mean horizontal offset across all matched features was found to be less than 30 cm, consistent with the native GSD of the OHRC instrument and with horizontal accuracy bounds reported for analogous high-resolution pushbroom stereo products [Kirk et al., 2008].

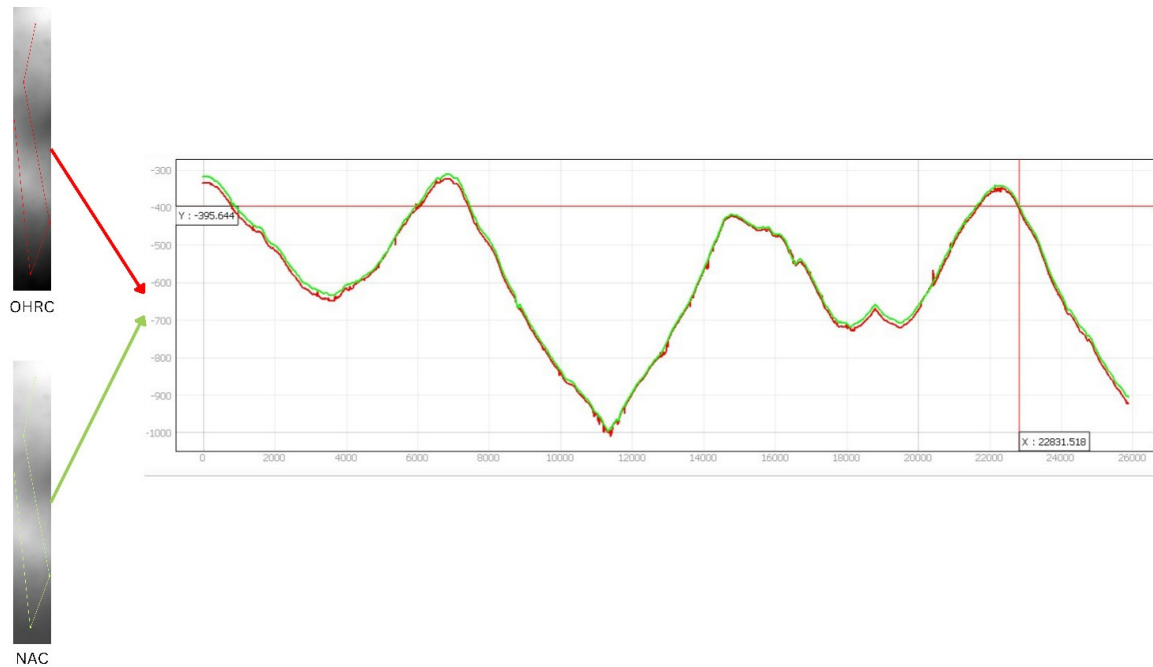


Figure 5: Terrain profile comparison across Region 4. Horizontal axis: distance along profile transect (m). Vertical axis: elevation (m). Red curve: OHRC DEM. Green curve: NAC DTM reference.

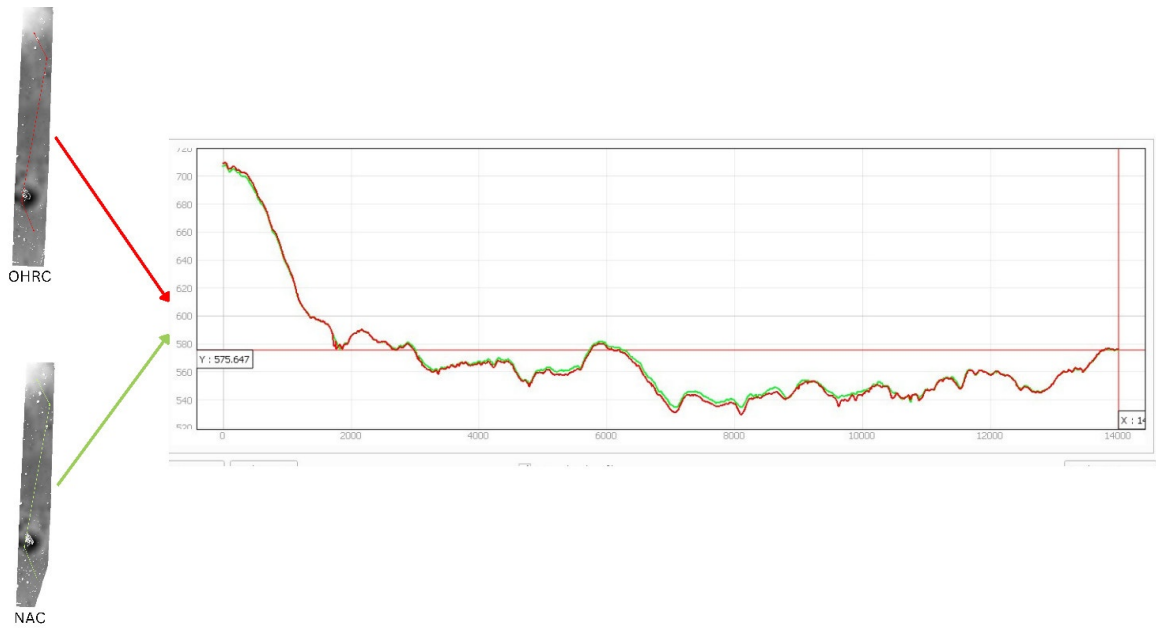


Figure 6: Terrain profile comparison across Region 1. Horizontal axis: distance along profile transect (m). Vertical axis: elevation (m). Red curve: OHRC DEM. Green curve: NAC DTM reference.

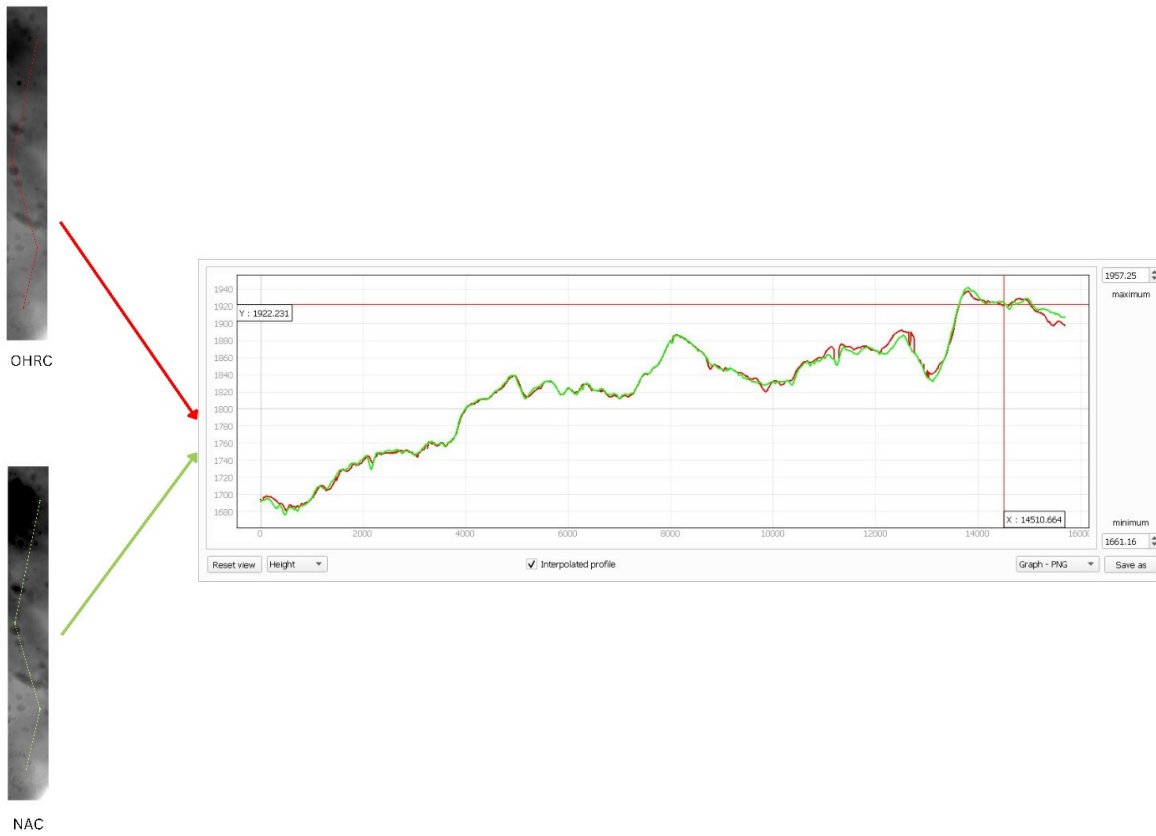


Figure 7: Terrain profile comparison across Region 2. Horizontal axis: distance along profile transect (m). Vertical axis: elevation (m). Red curve: OHRC DEM. Green curve: NAC DTM reference.

Elevation profile comparisons for three representative regions (4,1, and 2, respectively) are shown in Figs. 5–7.

## 5.2 Computational Performance

All processing was performed on a workstation equipped with an Intel Xeon Gold 6530 processor (128 logical cores) and 1 TB of RAM. Table 4 reports wall-clock timings for each major stage of the pipeline, measured across the five stereo pairs. The pre-processing stages, including `isisimport`, `spiceinit`, and ISD generation via `isd_generate`, are collectively lightweight, completing in approximately 1–2 min per stereo pair. Their cost is dominated by kernel database queries and JSON serialisation rather than computation, and scales only weakly with image size.

Bundle adjustment, which iterates a Levenberg–Marquardt optimiser over matched tie points until convergence or the 100-iteration limit is reached, required approximately 10–20 min per pair. This is consistent with reported runtimes for comparable pushbroom stereo datasets in the planetary photogrammetry literature [Beyer et al., 2018, Kirk et al., 2008].

The dominant cost is dense stereo correspondence (`parallel_stereo`), which ran for approximately 10–30 min per pair, depending primarily on image overlap area and disparity-search range. Point cloud rasterisation (`point2dem`) required 30 min to 2 h per pair, with runtime governed by the output grid resolution; finer grids at sub-30 cm spacing incurred the longest runtimes.

Table 4: Approximate wall-clock runtimes per stereo pair for each pipeline stage. Hardware: Intel Xeon Gold 6530  $\times$  128 cores, 1 TB RAM.

Pipeline Stage	Tool(s)	Runtime (per pair)
Data ingest & SPICE init	<code>isisimport</code> , <code>spiceinit</code>	$\sim$ 1–2 min
Sensor model generation	<code>isd_generate</code> (ALE)	<1 min
Bundle adjustment	<code>bundle_adjust</code>	$\sim$ 10–20 min
Dense stereo correspondence	<code>parallel_stereo</code>	$\sim$ 10–30 min
Point cloud rasterisation	<code>point2dem</code>	$\sim$ 30 min – 2 h
ICP alignment & offset corr.	<code>pc_align</code> , QGIS	$\sim$ 5–15 min
<b>Total (approx.)</b>		$\sim$ 1–3 h

Stereo pair identification (convergence angle and B/H ratio computation from image metadata) is performed as a pre-pipeline analysis step and is not included in the above timings; it requires only seconds per candidate pair.

## 6 Discussion

The results demonstrate that sub-metre lunar DEMs can be generated from Chandrayaan-2 OHRC imagery using open-source photogrammetric tools, provided that two instrument-specific obstacles are addressed. The first is pipeline compatibility: the OHRC PDS4 data format and camera model are not supported out of the box by existing open-source stereo processing suites, and establishing this compatibility required developing a new import template and a CSM sensor configuration. The second is stereo pair identification: because OHRC images are not acquired as predefined stereo pairs, usable stereo combinations must be extracted entirely from orbital geometry parameters in individual image metadata, using B/H ratio and convergence angle as selection criteria.

The range of B/H ratios observed across Regions 1–4 (0.396–0.877) is comparable to values reported in HiRISE stereo studies [Kirk et al., 2008], confirming that the same geometric quality criteria are applicable to OHRC. For these four regions, where B/H falls within the conventionally recommended range of 0.3–1.0 [Toutin, 2002], stereo reconstruction produced DEMs with satisfactory spatial completeness and consistent validation metrics.

### Region 5 as a Limiting Case

Region 5 ( $\sim$ 4°N, 230°E) occupies a distinct position in the dataset. With a B/H ratio of 1.161 and a directly measured convergence angle of approximately 61°, this pair substantially exceeds the commonly recommended B/H ceiling of 1.0 [Toutin, 2002]. The high convergence angle translates directly into a large cross-view radiometric disparity: at  $\theta \approx 61^\circ$ , surface normals that are oblique to one camera are near-perpendicular to the other, causing marked differences in foreshortening, shadow extent, and local brightness across the two images. This radiometric mismatch severely

degrades the ability of the block matching algorithm to find reliable correspondences, particularly in shadow-affected regions and on surfaces with low photometric texture.

As a consequence, the DEM produced for Region 5, which was nominally the finest-resolution product in the dataset at 24 cm, exhibits a substantially elevated void fraction compared to Regions 1–4. The high nominal resolution is therefore of limited practical utility without extensive hole-filling from the NAC reference, which correspondingly reduces the fraction of the final terrain model that is genuinely OHRC-derived.

This observation provides an empirical upper bound for OHRC stereo pair selection. While B/H ratios up to approximately 1.16 are geometrically processable in the sense that `parallel_stereo` completes without error, a practical ceiling of  $B/H \lesssim 0.9$  is recommended for OHRC to ensure an acceptable balance between height sensitivity and spatial completeness of the output DEM. This threshold is consistent with the theoretical prediction from Eq. (5): at  $B/H=0.9$  the convergence angle is approximately  $48^\circ$ , which represents a reasonable upper bound for semi-global matching on high-contrast pushbroom imagery. The threshold may vary with terrain type and solar illumination conditions, and its refinement over a larger sample of pairs is left to future work.

Region 5 is retained in both dataset tables and included in the multi-panel DEM figure (Fig. 2) as a documented negative result. Its inclusion is intentional: it serves as a concrete illustration of the B/H upper-bound effect and provides a reference point for future studies that may wish to evaluate more aggressive stereo geometries with improved matching strategies such as deep-learning-based correspondence networks.

### Iterative Refinement via ICP-Informed Bundle Adjustment Re-Pass

Beyond the baseline pipeline described in Section 4, an optional iterative refinement procedure was explored as an additional exercise on selected regions. In the standard pipeline, ICP alignment corrects the absolute position of the reconstructed point cloud by estimating a rigid transformation against the NAC reference. However, this correction is applied post-reconstruction and does not propagate back into the photogrammetric camera models. As a consequence, any residual geometric inconsistency between the two cameras, that is small enough to survive the first bundle adjustment pass but detectable once a reference-aligned DEM is available, remains embedded in the camera pointing solution.

The refinement procedure closes this loop. The ICP-derived transformation matrix, which encodes the residual offset between the initial OHRC reconstruction and the NAC reference frame, is used to constrain a second bundle adjustment pass. With this geometry-informed initialisation, the optimiser converges to a camera solution that is more tightly anchored to the absolute reference frame than was achievable with SPICE-only initialisation. Dense stereo is then re-run under the refined camera models, and a new DEM is gridded using an expanded interpolation search radius to recover valid elevations in regions that were voids in the initial reconstruction. This expanded-radius gridding is particularly effective at filling isolated no-data pixels surrounded by valid measurements (gaps that arise not from systematic shadow or texture failure but from marginal correspondence scores near the stereo matching threshold).

The qualitative outcome of this procedure was a measurable improvement in spatial completeness: regions that had previously required NAC infill were recovered as genuinely OHRC-derived elevations, increasing the fraction of the final DEM that carries sub-metre native resolution. This improvement was achieved without introducing any additional external data source, relying entirely on the self-consistency between the initial reconstruction and the NAC reference as a geometric constraint. The full quantitative characterisation of the accuracy improvement attributable to this refinement pass is left to future work, where it will be evaluated systematically across a broader set of stereo pairs.

### Region-of-Interest Cropping for Targeted Reconstruction

A practical consideration in processing high-resolution OHRC imagery is that the full image swath is rarely of uniform scientific interest, and running dense stereo over the entire frame incurs unnecessary computational cost. To address this, a region-of-interest (ROI) approach was adopted in which only a user-selected sub-window of each image was passed to the stereo pipeline, rather than cropping the image files themselves.

ROI selection was performed interactively using `stereo_gui`, the graphical front-end provided by ASP, which allows the operator to inspect both images of a stereo pair simultaneously, identify the region of overlap containing the terrain of interest, and record the pixel coordinates of the desired sub-window. Alternatively, ROI bounds can be derived analytically by mapprojecting the images onto a reference terrain model and identifying the overlap footprint in geographic coordinates. The selected sub-window extents were then passed directly to `parallel_stereo` via the `-left-image-crop-win` and `-right-image-crop-win` parameters, each specified as  $\langle x_{\min}, y_{\min}, \text{width}, \text{height} \rangle$  in pixel coordinates. This approach avoids any modification of the source image files and preserves the full SPICE-based camera geometry, since the crop parameters are applied internally during stereo preprocessing.

The resulting DEM covers only the selected sub-region, with a corresponding reduction in processing time proportional to the area of the crop window relative to the full image. Furthermore, the number of valid pixels obtained also increases substantially, as a result of the selected regions being appropriately illuminated. It should be noted that the reconstructed DEM may appear geometrically offset relative to the raw cropped image chips when displayed together: the image chips retain their native pixel coordinate system, whereas the DEM is a georeferenced product whose spatial position is determined by the SPICE ephemeris, CSM camera model, and bundle-adjusted camera states established in earlier pipeline stages. The apparent tilt between the DEM and the source imagery is therefore not a reconstruction artefact but a consequence of correct geopositioning — the DEM is registered to the lunar body-fixed frame, while the image chips are not. This is illustrated in Fig. 8, which shows the generated DEM alongside the left and right cropped image chips for a selected patch from the images of Region 1 (1).

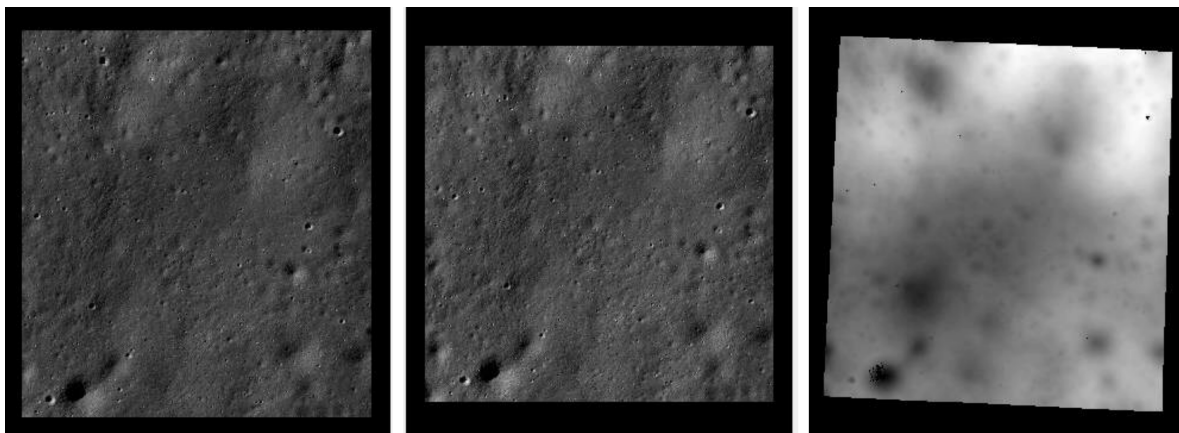


Figure 8: Region-of-interest stereo reconstruction. Left and centre: the left-camera and right-camera cropped image chips (run-L\_cropped and run-R\_cropped) in native pixel coordinates. Right: the reconstructed DEM for the same region.

## 7 Conclusion

This study presents the first framework for generating and metrologically validating sub-metre lunar DEMs from Chandrayaan-2 OHRC multi-view imagery using open-source photogrammetric tools. The work overcomes two previously unsolved obstacles: enabling open-source pipeline compatibility for the OHRC instrument through a new PDS4 import template and CSM camera configuration, and identifying viable stereo pairs from non-paired image archives using baseline-to-height ratio and convergence angle analysis. Stereo reconstruction is performed for five geographically distributed lunar regions, yielding DEMs at resolutions between 24 and 54 cm — the highest reported from OHRC data, and covering substantially more sites than prior efforts. Absolute elevation consistency is established through ICP alignment with NAC reference terrain, residual biases are corrected from profile comparison, and continuous coverage is achieved through priority-based mosaicing. Horizontal accuracy, assessed by planimetric feature matching against the NAC DTM hillshade at 5–10 features per region, was found to be less than 30 cm, consistent with the native GSD of the OHRC instrument. Vertical accuracy against the NAC reference at native resolution yields a mean RMSE of 5.85 m across Regions 1, 2, and 4. Region 5 is documented as a limiting case, establishing an empirical B/H ceiling of approximately 0.9 for reliable OHRC stereo reconstruction.

Future work will extend coverage to broader lunar regions, perform shape-from-shading refinement, and apply the resulting terrain products to landing site hazard analysis.

## Acknowledgements

The authors thank the Director, Space Applications Centre (SAC), ISRO, for providing the opportunity to undertake this work. The authors are grateful to the Deputy Director, SIPA, for his encouragement and support, and acknowledge the guidance and support provided by the Head, PSPD.

The authors also thank ISRO for providing open access to the Chandrayaan-2 OHRC imagery and SPICE kernel archive through the ISSDC PRADAN portal. The authors also acknowledge the NASA Ames Stereo Pipeline (ASP) team and

the USGS ISIS community for their open-source software and providing the development support for Chandrayaan-2 data, which were integral to this work.

## References

- C. H. Acton. Ancillary data services of NASA's navigation and ancillary information facility. *Planetary and Space Science*, 44(1):65–70, 1996. doi:10.1016/0032-0633(95)00107-7.
- S. Agarwal, K. Mierle, and The Ceres Solver Team. Ceres solver, 2022. URL <http://ceres-solver.org>.
- H. Araki, S. Tazawa, H. Noda, et al. Lunar global shape and polar topography derived from Kaguya-SELENE laser altimetry. *Science*, 323(5916):897–900, 2009. doi:10.1126/science.1164146.
- MK Barker, E Mazarico, GA Neumann, MT Zuber, Junichi Haruyama, and DE Smith. A new lunar digital elevation model from the lunar orbiter laser altimeter and selene terrain camera. *Icarus*, 273:346–355, 2016.
- KJ Becker, BA Archinal, TH Hare, RL Kirk, E Howington-Kraus, MS Robinson, and MR Rosiek. Criteria for automated identification of stereo image pairs. In *46th Annual Lunar and Planetary Science Conference*, number 1832, page 2703, 2015.
- P. J. Besl and N. D. McKay. A method for registration of 3-D shapes. *IEEE Transactions on Pattern Analysis and Machine Intelligence*, 14(2):239–256, 1992. doi:10.1109/34.121791.
- R. A. Beyer, O. Alexandrov, and S. McMichael. The Ames Stereo Pipeline: NASA's open-source software for deriving and processing terrain data. *Earth and Space Science*, 5(9):537–548, 2018. doi:10.1029/2018EA000409.
- A. R. Chowdhury, M. Saxena, A. Kumar, S. R. Joshi, A. Dagar, M. Mittal, S. Kirkire, J. Desai, D. Shah, J. C. Karelia, and A. Kumar. Orbiter high resolution camera onboard Chandrayaan-2 orbiter. *Current Science*, 118(4):560–565, 2020. doi:10.18520/cs/v118/i4/560-565.
- Community Sensor Model Working Group. Community sensor model technical requirements document. Technical Report NGA.STND.0017 3.0, National Geospatial-Intelligence Agency, Springfield, VA, 2015.
- Gabriele Facciolo, Carlo De Franchis, and Enric Meinhardt. Mgm: A significantly more global matching for stereovision. In *BMVC 2015*, 2015.
- Lisa Gaddis, J Anderson, K Becker, T Becker, D Cook, K Edwards, E Eliason, T Hare, H Kieffer, EM Lee, et al. An overview of the integrated software for imaging spectrometers (isis). In *28th Annual Lunar and Planetary Science Conference, March 17-21, 1997, Houston, TX, p. 387.*, volume 28, page 387, 1997.
- Sajid Ghuffar. Dem generation from multi satellite planetscope imagery. *Remote Sensing*, 10(9):1462, 2018.
- A. Gupta, K. Suresh, A. K. Prashar, K. V. Iyer, A. Suhail, S. Verma, B. Islam, H. K. Lalwani, and T. P. Srinivasan. High resolution DEM generation from Chandrayaan-2 orbiter high resolution camera images. In *52nd Lunar and Planetary Science Conference*, LPI Contribution No. 2548, page 1396, 2021.
- Richard Hartley and Andrew Zisserman. *Multiple view geometry in computer vision*. Cambridge university press, 2003.
- Hiroyuki Hasegawa, Kaoru Matsuo, Mamoru Koarai, Nobuyuki Watanabe, Hiroshi Masaharu, and Yoshikazu Fukushima. Dem accuracy and the base to height (b/h) ratio of stereo images. *International Archives of Photogrammetry and Remote Sensing*, 33(B4/1; PART 4):356–359, 2000.
- Adam J Hepburn, Tom Holt, Bryn Hubbard, and Felix Ng. Creating hirise digital elevation models for mars using the open-source ames stereo pipeline. *Geoscientific Instrumentation, Methods and Data Systems*, 8(2):293–313, 2019.
- Indian Space Research Organisation. Chandrayaan-2 orbiter payload data user handbook. Technical report, ISRO, 2019.
- Kannan V Iyer, Medha S Alurkar, Ajay Kumar Prashar, K Suresh, et al. Path tracing of the chandrayaan-3 rover from ohrc images. *Current Science (00113891)*, 128(6), 2025.
- R. L. Kirk, E. Howington-Kraus, M. R. Rosiek, et al. Ultrahigh resolution topographic mapping of Mars with MRO HiRISE stereo images: Meter-scale slopes of candidate Phoenix landing sites. In *Journal of Geophysical Research: Planets*, volume 113, 2008. doi:10.1029/2007JE003000.
- JR Laura, Jesse Mapel, and T Hare. Planetary sensor models interoperability using the community sensor model specification. *Earth and Space Science*, 7(6):e2019EA000713, 2020. doi:10.1029/2019EA000713.
- Pengying Liu, Xun Geng, Tao Li, Jiujiang Zhang, Yuying Wang, Zhen Peng, Yinhui Wang, Xin Ma, and Qiudong Wang. The generation of high-resolution mapping products for the lunar south pole using photogrammetry and photogrammetry. *Remote Sensing*, 16(12):2097, 2024. doi:10.3390/rs16122097.

- Zachary M Moratto, Michael J Broxton, Ross A Beyer, Mike Lundy, and Kyle Husmann. Ames stereo pipeline, nasa's open source automated stereogrammetry software. In *41st Annual Lunar and Planetary Science Conference*, number 1533, page 2364, 2010.
- M. S. Robinson, S. M. Brylow, M. Tschimmel, et al. Lunar reconnaissance orbiter camera (LROC) instrument overview. *Space Science Reviews*, 150:81–124, 2010. doi:10.1007/s11214-010-9634-2.
- D. E. Shean, O. Alexandrov, Z. M. Moratto, et al. An automated, open-source pipeline for mass production of digital elevation models (DEMs) from very-high-resolution commercial stereo satellite imagery. *ISPRS Journal of Photogrammetry and Remote Sensing*, 116:101–117, 2016. doi:10.1016/j.isprsjprs.2016.03.012.
- D. E. Smith, M. T. Zuber, G. A. Neumann, et al. Initial observations from the lunar orbiter laser altimeter (LOLA). *Geophysical Research Letters*, 37(18), 2010. doi:10.1029/2010GL043751.
- E. K. Stathopoulou et al. Open-source image-based 3D reconstruction pipelines: review, comparison and evaluation. In *ISPRS Ann. Photogramm. Remote Sens. Spat. Inf. Sci.*, volume IV-2/W6, pages 331–338, 2019.
- T. Toutin. Three-dimensional topographic mapping with ASTER stereo data in rugged topography. *IEEE Transactions on Geoscience and Remote Sensing*, 40(10):2241–2247, 2002. doi:10.1109/TGRS.2002.802878.